The synaptonemal complex controls cis- versus trans-interference in coarsening-based meiotic crossover patterning

John A Fozard[1], Chris Morgan[2,*], Martin Howard[1,*]

[1] Computational and Systems Biology and [2]Cell and Developmental Biology, John Innes Centre, Norwich Research Park, Norwich NR4 7UH, UK

* Co-corresponding authors: chris.morgan@jic.ac.uk, martin.howard@jic.ac.uk

Abstract

The shuffling of genetic material facilitated by meiotic crossovers is a critical driver of genetic variation. Therefore, the number and positions of crossover events must be carefully controlled. In *Arabidopsis,* an obligate crossover and repression of nearby crossovers on each chromosome pair are abolished in mutants that lack the synaptonemal complex (SC), a conserved protein scaffold. We use mathematical modelling and quantitative super-resolution microscopy to explore and mechanistically explain meiotic crossover pattering in *Arabidopsis zyp1* mutants, that lack an SC. We develop an SC mutant coarsening model in which crossover precursors globally compete for a limited pool of the pro-crossover factor HEI10, with dynamic HEI10 exchange mediated through the nucleoplasm. We demonstrate that this model is capable of quantitatively reproducing and predicting experimental crossover patterning and HEI10 foci intensity data. Our results reveal that regulation of the number of crossovers within a cell in SC mutants (“trans-interference”), and inhibition of nearby crossovers on the same chromosome in wild-type cells (“cis-interference”), likely act through the same underlying coarsening mechanism, differing only in the spatial compartment through which the pro-crossover factor diffuses. The spatial compartment used is controlled by the SC, which therefore acts as a critical regulator of cis- versus trans-interference.

Introduction

During meiotic prophase I, pairs of threadlike homologous chromosomes are tethered together through the formation of a protein scaffold called the synaptonemal complex (SC) (Page and Hawley, 2004). Prior to SC formation, programmed double strand breaks (DSBs) form along the length of the chromosomal DNA (Gray and Cohen, 2016; Hunter, 2015). DSBs are then repaired via the formation of recombination-intermediate (RI) DNA joint-molecules, as either non-crossovers (NCOs) or crossovers (COs) (Gray and Cohen, 2016; Hunter, 2015). In most species, the number of RIs repaired as NCOs vastly outnumbers those repaired as COs (Gray and Cohen, 2016; Hunter, 2015). Importantly, nearby pairs of COs on the same chromosome are less likely to occur than more distant pairs, but each pair of chromosomes always receives at least one CO. These phenomena are known as 'crossover interference' and 'crossover assurance', respectively (Jones and Franklin, 2006; Otto and Payseur, 2019; Sturtevant, 1915; von Diezmann and Rog, 2021; Zickler and Kleckner, 2016).

Recently, we introduced a mechanistic coarsening model that quantitatively explains CO interference, CO assurance and other CO patterning features in wild-type *Arabidopsis thaliana* (Morgan et al., 2021). In our coarsening model, the pro-CO protein HEI10 (Chelysheva et al., 2012; Ziolkowski et al., 2017) can diffuse along synapsed homolog bivalents and can reversibly bind into immobile clusters at RI sites. Conservation of the total amount of HEI10 on individual bivalents, along with an unbinding escape rate from RIs that decreases as more HEI10 locally accumulates, causes the system to coarsen. By the end of the pachytene substage of prophase I, HEI10 is retained at only a small number of predominantly distantly-spaced RIs, each with high levels of HEI10, which are then designated to become COs (Morgan et al., 2021). A similar model was subsequently proposed to underlie CO patterning in *C. elegans* (Zhang et al., 2021), suggesting that this molecular coarsening paradigm represents a conserved feature of meiotic CO control.

The coarsening model fundamentally relies on the retention of HEI10 molecules on synapsed bivalent chromosomes, and redistribution of HEI10 molecules by diffusion along the bivalents. Work in *C. elegans* points to the SC acting as a conduit, or channel, through which HEI10 molecules can diffuse, promoting coarsening in cis along individual bivalents. Consistently, in *C. elegans*, the SC is known to have liquid-crystal like properties that can spatially compartmentalise pro-CO proteins (Rog et al., 2017; Zhang et al., 2018). Furthermore, innovative live-cell imaging experiments have recently directly demonstrated that ZHP-3, a HEI10 ortholog, can diffuse along the SC (Stauffer et al., 2019; Zhang et al., 2021). In *Arabidopsis*, it was also recently shown that CO interference and assurance are abolished in plants lacking the SC transverse filament protein, ZYP1(Capilla-Pérez et al., 2021; France et al., 2021). These observations suggest that the SC plays a direct role in mediating crossover patterning dynamics.

In this work, we therefore develop a new coarsening model for crossover interference in the absence of an intact SC, and use it to explore the regulation of crossover number and position in *Arabidopsis* SC mutants. In this new model, due to the lack of an SC, HEI10 molecules are no longer restricted to diffuse in cis along individual bivalents. Instead, HEI10 is assumed to diffuse through a communal nucleoplasm, generating competition for HEI10 between RIs located on different bivalents. Similarly, in *C. elegans*, it has previously been suggested that the SC functions to prevent exchange of recombination proteins between RIs via the nucleoplasm (Rog et al., 2017; Zhang et al., 2021, 2018). Using our model, we provide a mechanistic explanation for why SC mutants lose both CO interference and assurance. Intriguingly, we also reveal an additional layer of crossover control: SC-mutants lose positional effects that are determined by 'cis-interference' (along individual chromosome pairs), but exhibit constraints on total crossover number per-cell that are governed by

75 ‘trans-interference’ (between different chromosome pairs). Overall, our results demonstrate a
76 critical role for the SC in controlling these cis- versus trans- interference effects.
77

78 Results

79

80 A nucleoplasm-mediated coarsening model for crossover patterning without the SC

81

82 The SC likely acts as a conduit for HEI10 diffusion along synapsed pachytene bivalents (Morgan et al.,
83 2021; Rog et al., 2017; Zhang et al., 2021, 2018). Without an SC, we postulated that HEI10 diffusion
84 could instead occur through the nucleoplasm, with little or no movement along chromosomes, as
85 has also previously been suggested from work in *C. elegans* (Zhang et al., 2021). We therefore
86 investigated this hypothesis by developing a new coarsening model for crossover interference
87 without an SC. This ‘nucleoplasmic coarsening’ model incorporates the processes shown in Figure 1.
88 There are 5 pairs of homologous chromosomes in each cell. At the start of the simulation each
89 chromosome pair (CP) is assigned a random length, drawn from experimentally measured length
90 distributions. We then place RIs at random positions along the length of each CP, with a constant
91 probability per unit length.

92 In this model, HEI10 is able to move from the nucleoplasmic pool to the HEI10 clusters at each of the
93 RIs. It can also escape from the RI clusters back into the nucleoplasmic pool, at a rate which depends
94 on the amount of HEI10 within that RI cluster. Similar to previous work, this rate is chosen to have
95 the form shown in Figure 1C,D, decreasing as the amount of HEI10 within the RI compartment
96 increases. Random amounts of HEI10 are initially loaded at each RI. These initial loading amounts are
97 multiplied by a multiplicative factor shown in Figure 1F, increasing loading near CP ends. HEI10 is
98 also initially present in the nucleoplasmic pool, at a constant amount that was chosen to be similar
99 to the total amount of HEI10 loaded onto all the synaptonemal complexes within each cell in our
100 original wild-type coarsening model (Morgan et al., 2021).
101

102 This model differs from our earlier model for meiosis in wild-type plants, in which HEI10 was able to
103 diffuse along the SC between RIs (Morgan et al., 2021). There, the total amount of HEI10 for a pair of
104 chromosomes was conserved. Here, the total amount of HEI10 within the cell is instead conserved.
105 However, as in the earlier model, if the total amount of HEI10 is sufficiently high then a uniform
106 steady state becomes unstable and the system progressively coarsens, with RIs with more HEI10
107 growing at the expense of those with less. Eventually, the majority of the HEI10 will accumulate into
108 a single focus per cell, but the limited duration of pachytene means that this process does not
109 complete, and instead there are a number of RIs with significant levels of HEI10 at the end of the
110 simulation.

111 Nucleoplasmic coarsening model generates trans-interference of COs

112 To determine whether the nucleoplasmic coarsening model was capable of explaining CO patterning
113 in SC deficient *Arabidopsis*, we first sought to fit the model to existing experimental data on CO
114 frequency from *Arabidopsis zyp1* null mutants, which lack an SC. These data include total CO number
115 and number of homologs without a CO (Figure 2A,B).

116 By counting the number of MLH1 foci in late-prophase I cells in 7 different Col-0 *zyp1* null mutant
117 lines, it was previously (Capilla-Pérez et al., 2021) found that there was a ~50% increase in the
118 predominant class I COs in these mutants compared with wild-type (data from (Capilla-Pérez et al.,
119 2021), shown in Figure 2A). Also, by analysing DAPI stained metaphase I cells, it was found (Capilla-
120 Pérez et al., 2021) that ~10% of metaphase I cells contained a pair of univalent chromosomes, which

form when homologs fail to form a single CO, indicating an absence of CO assurance (data from (Capilla-Pérez et al., 2021), shown in Figure 2B). Importantly, we found that the nucleoplasmic coarsening model was capable of recapitulating these two findings (Figure 2A, B). The number of COs per cell was slightly less dispersed, with a lower sample variance, within our model than in the experimental data. This reduction is likely because the experimental data is pooled from multiple different mutant lines, each of which has a slightly different mean number of COs per cell (Capilla-Pérez et al., 2021), thereby generating a broader distribution. The expected frequency of univalents is also slightly higher in our simulation outputs than in the experimental data, but this is again expected as chiasma number in metaphase I cells (that were used for the experimental analysis) are influenced by both class I and class II CO numbers, whereas the nucleoplasmic coarsening model only simulates CO patterning via the (dominant) class I pathway. Assuming ~2 additional class II COs per cell (Mercier et al., 2005) are distributed randomly among the five CPs, in a simple estimation we would expect the univalent frequency in our model output to drop by ~40% (from 20% of cells to 12% of cells containing one or more univalent). However, univalents are more likely to be associated with the shorter chromosomes, as they have fewer RIs. This effect slightly reduces how much the addition of class II crossovers decreases the frequency of cells with one or more univalent. In our simulations we thus find a value of ~14%, similar to but slightly higher than previous observations (~11%).

Using the nucleoplasmic coarsening model, we were also able to simulate the distribution of crossovers on each of the five *Arabidopsis* chromosomes (Figure 2C). We found that the distribution of the number of crossovers on each chromosome is close to a Poisson distribution, with nearly equal mean and variance. Processes that occur at a constant probability per unit space or time, when integrated over a fixed interval, have a Poisson distribution (Haldane, 1931). Hence, as expected, CO-interference along each chromosome (cis-interference) is not present in this model. These findings are consistent with a previous genetic analysis by (Capilla-Pérez et al., 2021), which found that the distribution of CO numbers on individual chromosomes did not deviate from a Poisson distribution.

Paradoxically, while the distribution of CO numbers on individual chromosomes in our simulations closely followed a Poisson distribution, the total number of COs per cell did not and was found to be significantly under-dispersed relative to a Poisson distribution (Figure 2A). Compellingly, we found that this sub-Poissonian distribution of total CO numbers per cell fit well with the experimental data from (Capilla-Pérez et al., 2021) (Figure 2A), although this experimental under-dispersion was not previously highlighted. In the model, the total number of crossovers in each cell is regulated through global competition for HEI10, thereby leading to under-dispersion, despite the fact that there is no control on the number of crossovers on each CP. We refer to this regulatory phenomenon as 'trans-interference' in order to differentiate it from the spatial patterning of COs along individual chromosomes ('cis-interference') in the wild-type. Cis-interference depends on competition for a limited pool of HEI10 that is independently associated with each CP, resulting in a sub-Poisson distribution of CO numbers on each chromosome. Trans-interference depends on competition for a limited nucleoplasmic pool of HEI10 within a cell, as well as regulation of cell-to-cell total HEI10 amounts, resulting in a sub-Poissonian distribution of CO numbers in each cell. However, in trans-interference, the amount of HEI10 associated with each CP within the cell can fluctuate due to diffusion of HEI10 between RIs on different CPs through the communal nucleoplasmic pool, resulting in a close-to-Poissonian distribution of CO numbers on each chromosome.

We also found that the coarsening dynamics within the nucleoplasmic coarsening model were capable of occurring within the limited ~10h duration of the pachytene substage of prophase I in

167 *Arabidopsis* (Prusicki et al., 2019) (Figure 2D). Overall, we find that the nucleoplasmic coarsening
168 model fits well with prior data on CO numbers in SC mutants, giving strong support to the hypothesis
169 of nucleoplasmic HEI10 exchange.

170 Super-resolution imaging of HEI10 in SC-defective cells

171 As described above, previous studies have used HEI10 and MLH1 focus counts per cell, alongside
172 genetic analyses, to examine the effects of SC absence on CO frequency in *Arabidopsis.* However, the
173 material positioning of recombination sites (in units of microns) along prophase I chromosomes has
174 not yet been cytologically investigated. This is particularly important because, as argued in (Zickler
175 and Kleckner, 2016), the optimal metric for measuring CO interference is microns of axis length.
176 Additionally, as shown previously, correlations between HEI10 focal intensity and foci number or
177 position can be detected that provide strong experimental support for the coarsening model
178 (Morgan et al., 2021).

179 We therefore used super-resolution microscopy and a bespoke image-analysis pipeline to quantify
180 the position and intensity of late-HEI10 foci (that are known to mark the positions of class I COs
181 (Chelysheva et al., 2012)), along late prophase I chromosomes in wild-type and *zyp1a-2/zyp1b-1* SC
182 null mutant lines (previously characterised in (France et al., 2021)) (Figure 3A,B). Late-prophase I
183 cells from wild-type and *zyp1a-2/zyp1b-1* plants were stained for SMC3 (Lam et al., 2005) and HEI10
184 (Chelysheva et al., 2012), which label the meiotic axis and putative CO sites, respectively, and
185 imaged using 3D-SIM microscopy. In total, we imaged 10 cells from 4 wild-type plants and 14 cells
186 from 4 *zyp1a-2/zyp1b-1* plants, which provided sufficient data to quantitively compare with model
187 simulations. By tracing along the linear SMC3 signals, using the SNT plugin to FIJI (Arshadi et al.,
188 2021), we were able to segment the 10 axial elements in each cell (Figure 3A,B, top right panels). In
189 accordance with previous studies, we found that axial elements of homologous chromosomes were
190 tightly juxtaposed along their entire lengths in wild-type cells, whilst in the *zyp1a-2/zyp1b-1* line the
191 axes were only loosely paired along their lengths (Figure 3A,B, bottom rows), with the majority of
192 HEI10 foci being clearly located between the two homologous axes at an equivalent position along
193 their length (Figure 3A,B, right hand boxes) (Capilla-Pérez et al., 2021; France et al., 2021). Once the
194 paths of segmented axes had been extracted from the images, we were then able to use an
195 automated image analysis pipeline to assign HEI10 foci to specific positions along individual axes
196 based on their local proximity to those regions (Materials and Methods).

197 Nucleoplasmic coarsening model successfully predicts HEI10 foci patterning and intensities

198 Using the experimental cytology and image analysis described above, we were able to construct
199 cytological recombination maps from both wild-type and *zyp1a-2/zyp1b-1* SC null mutant plants
200 (Figure 4A). In the wild-type we found an average of 9.0 late-HEI10 foci per cell, while in the *zyp1a-*
201 *2/zyp1b-1* line we found an average of 18.7 late-HEI10 foci per cell, which was broadly consistent
202 with previous cytological analyses of CO numbers in similar lines (Capilla-Pérez et al., 2021; France et
203 al., 2021).

204 When analysing the relative distribution of all late-HEI10 foci along CPs, we found that in the *zyp1a-*
205 *2/zyp1b-1* line the distribution of late-HEI10 foci was shifted towards more distal positions, nearer
206 the chromosome ends, when compared with the wild-type, which was also consistent with previous
207 genetic analysis of *zyp1* null mutants (Capilla-Pérez et al., 2021) (Figure 4A). Importantly, the
208 nucleoplasmic coarsening model was capable of recapitulating this distribution, with a preference
209 for forming COs in more distal regions (Figure 4A). Such increases are a direct consequence of the
210 additional initial HEI10 loading applied to RIs near chromosome ends, which was a parameter that

211 was included in the original coarsening model (Morgan et al., 2021). Note that the extra loading here
212 (up to 25% on the most distal 60% of each CP) is lower and more spread than that used in the
213 original model (up to 100% on the most distal 20%). The increased end-loading of HEI10 was
214 included in the original model because the dynamics of cis-coarsening naturally decrease the
215 likelihood of RIs close to chromosome ends forming COs. As there is an absence of cis-coarsening in
216 the nucleoplasmic coarsening model, each RI is equally capable of forming a CO regardless of its
217 position. Thus, even though there is less pronounced HEI10 end-loading in our nucleoplasmic
218 coarsening model compared with our original model, this lower end-bias still causes a relative
219 increase in distally positioned COs under nucleoplasmic coarsening conditions. In the original
220 coarsening model, we hypothesised this end bias results from preferential synapsis near the
221 chromosome ends. In the absence of an SC there is obviously no synapsis, which explains why this
222 end loading is muted. However, the preferential pairing of telomeres (to form the meiotic bouquet)
223 (Varas et al., 2015), which presumably still happens in the absence of an SC, may explain why a
224 smaller end-bias for HEI10 loading persists.

225 We also examined the spacing between adjacent late-HEI10 foci on the same CP. In the wild-type,
226 we found a scarcity of closely spaced crossovers, with a greater frequency of distantly spaced COs,
227 reflecting the action of cis-interference (Figure 4B). This was consistent with our previous analysis of
228 wild-type CO patterning (albeit noisier due to the smaller sample size in this study) (Morgan et al.,
229 2021). In the *zyp1a-2/zyp1b-1* line, however, we found a very high frequency of closely spaced
230 crossovers, with a diminishing number of distantly spaced COs (Figure 4B). This behaviour reflects an
231 absence of cis-interference, and provides strong cytological support for previous conclusions drawn
232 from genetic experiments in *zyp1* null mutants (Capilla-Pérez et al., 2021). In this instance, the
233 nucleoplasmic coarsening model was fully capable of predicting this pattern of closely spaced COs,
234 without additional parameterisation, validating the model and reflecting an absence of cis-
235 interference (Figure 4B).

236 In addition to the late-HEI10 focus positioning data, we were also able to extract fluorescence
237 intensity measurements from each HEI10 focus in our imaging data. In wild-type *Arabidopsis,* we
238 previously showed that the normalized intensity of individual late HEI10 foci is negatively correlated
239 with the number of foci per bivalent, which is consistent with a cis-coarsening process (Morgan et
240 al., 2021). Here, we again identified such a correlation in wild-type plants (Figure 4C). However, we
241 did not find such a negative correlation in *zyp1a-2/zyp1b-1* mutants (Figure 4C). This would be
242 expected from a nucleoplasmic coarsening model as, in this scenario, HEI10 is equally capable of
243 diffusing through the nucleoplasm from any one RI to any other RI, regardless of whether the other
244 RI is located on the same CP or a different CP (see Figure 1A,B). Indeed, simulations of the
245 nucleoplasmic coarsening model again predicted these findings without the need for additional
246 parameterisation and produced comparable results to the *zyp1a-2/zyp1b-1* line (Figure 4C).
247

248 Discussion

249

250 It was recently shown that the SC, a highly conserved and prominent feature of meiotic prophase I,
251 is required to promote CO interference and CO assurance in *Arabidopsis thaliana* (Capilla-Pérez et
252 al., 2021; France et al., 2021). However, the mechanistic details of precisely how the SC plays a role
253 in mediating interference remained obscure. Here, using a combination of modelling and super-
254 resolution microscopy, we have shown that CO patterning in the absence of an SC is consistent with
255 a coarsening model for CO interference. Previously, we introduced a mechanistic, mathematical
256 coarsening model that could explain CO patterning in wild-type *Arabidopsis*, as well as in HEI10 over
257 and under-expressor lines (Morgan et al., 2021). Here, we make just one major change to the model

258 for SC mutants: that HEI10 can now exchange through a nucleoplasmic pool rather than being
259 restricted to individual chromosome pairs, as in the wild-type. With this biologically plausible
260 modification, the coarsening model is now also capable of explaining why SC mutants lack CO
261 assurance and CO interference in *Arabidopsis*. Additionally, the model successfully predicts
262 previously unexplored observations in SC mutants, including the pattern of closely-spaced COs and
263 the absence of an anticorrelation between HEI10 focal intensity and focus number per
264 chromosome pair. A similar function of the SC, in preventing the diffusion of recombination
265 proteins via the nucleoplasm, has been proposed in *C. elegans* (Rog et al., 2017; Zhang et al., 2021,
266 2018). However, unlike in *C. elegans* where successful CO formation depends upon SC formation
267 (Colaiácovo et al., 2003), in *Arabidopsis* SC formation and CO formation can be uncoupled (Capilla-
268 Pérez et al., 2021; France et al., 2021), making *Arabidopsis* an excellent system for demonstrating
269 the effects of nucleoplasmic coarsening. Overall, our work highlights the critical role of the SC in
270 controlling the spatial compartment through which HEI10 diffuses and therefore in selecting
271 whether cis- versus trans- interference effects occur in crossover patterning.

272 We have used the term trans-interference to refer to the regulation of total CO numbers within a
273 cell in the absence of the regulated spatial patterning of COs along individual chromosomes (cis-
274 interference). In wild-type cells, cis-interference operating along individual chromosomes regulates
275 total CO numbers along each chromosome. In turn, the combined effect of cis-interference
276 operating along all chromosomes within a cell causes global regulation of the total number of COs
277 within a cell, with the variance in total CO number per cell being close to the sum of the per
278 chromosome variances. SC mutants lose cis-interference but retain per-cell constraints on total CO
279 numbers via trans-interference, as evidenced by the Poissonian and sub-Poissonian distributions of
280 total CO numbers on individual chromosome pairs and in individual cells, respectively. In other
281 words, in an SC mutant, COs designated on different RIs are spatially independent from one another
282 but their numbers are not independent. As noted in (Crismani et al., 2021), an explanation for why
283 CO numbers are still relatively low (but still higher that wild-type) in SC mutants could be due to the
284 influence of a limiting trans-acting factor, such as HEI10. Similarly, in our modified coarsening model,
285 the limited nucleoplasmic pool of HEI10 explains why the distribution of total CO numbers per cell
286 remains sub-Poissonian. Importantly, caution should be exercised when interpreting sub-Poissonian
287 or Poissonian distributions of total CO number per cell as signs of functional or non-functional cis-
288 interference, respectively. As we show here, a sub-Poissonian distribution is perfectly compatible
289 with non-functional cis-interference.

290 The complex interplay between HEI10 mediated cis and trans-interference can also provide a
291 potential mechanistic explanation for other crossover phenomena, such as the interchromosomal
292 effect (Miller, 2020; Termolino et al., 2019).The interchromosomal effect describes the observation
293 that when one pair of homologs experiences a reduction in crossover frequency (due to a structural
294 variation, such as an inversion) this is accompanied by a corresponding increase in crossover
295 frequency on the other, structurally normal, homolog pairs (Miller, 2020; Termolino et al., 2019). In
296 this scenario, RIs may be inhibited from occurring normally at the sites of structural variations,
297 leading to a lower level of HEI10 in those regions. In turn, this could lead to a redistribution of the
298 limited pool of HEI10 to the other chromosomes, thus increasing the likelihood of those
299 chromosomes receiving additional COs.

300 Additionally, HEI10-coarsening could explain aspects of CO patterning in mutants that exhibit partial,
301 but incomplete, synapsis. For example, in *Arabidopsis axr1*, *pss1* and *asy1* mutants, incomplete
302 synapsis is associated with an abundance of closely spaced COs (Duroc et al., 2014; Jahns et al.,
303 2014; Lambing et al., 2020; Pochon et al., 2022). In this scenario, available HEI10 molecules could

still load on to the SC and undergo cis-coarsening, similar to the situation in the wild-type. However, if a wild-type level of HEI10 protein was loaded onto shorter stretches of SC, this would result in an increased concentration of HEI10 per micron of SC and, akin to the situation in a HEI10 over-expressor (Morgan et al., 2021), an increase in closely-spaced COs within those stretches.

In *Arabidopsis,* it was also found that heterochiasmy, the sex specific difference in CO frequency, is abolished in SC mutants (Capilla-Pérez et al., 2021). In wild-type *Arabidopsis*, female meiocytes have a reduced total CO frequency relative to male meiocytes, as well as a proportional decrease in total SC length (Drouaud et al., 2007; Giraut et al., 2011). Using the coarsening model, we previously demonstrated that heterochiasmy in *Arabidopsis* can be fully explained by simply altering the length of the SC in our model simulations (Morgan et al., 2021). Assuming female meiocytes also display a lack of synapsis and possess an RI frequency equivalent to their male counterparts in *zyp1* null mutants, we would not expect that female simulations of the nucleoplasmic coarsening model would differ from male simulations. Thus, a complete lack of heterochiasmy would be predicted. However, due to the technical challenges associated with performing immunocytological experiments in female *Arabidopsis* meiocytes*,* we acknowledge that this conclusion remains untested.

Together, the results we present here further reinforce the ability of the coarsening paradigm to explain numerous aspects of CO control in both wild-type and mutant *Arabidopsis* lines. These aspects include: CO placement, CO frequency, CO assurance, cis-interference, trans-interference, CO homeostasis, heterochiasmy, meiotic duration, interchromosomal effects and diverse HEI10 focal intensity measurements. Given the conserved nature of HEI10 (Agarwal and Roeder, 2000; Chelysheva et al., 2012; Jantsch et al., 2004; Lake et al., 2015; Qiao et al., 2014; Reynolds et al., 2013), and the discovery of similar coarsening mechanisms in *C. elegans* (Zhang et al., 2021), it is likely that similar mechanisms regulate these same crossover patterning phenomena in a wide variety of sexually reproducing eukaryotes.

Acknowledgments

We gratefully acknowledge James Higgins for providing the *zyp1a-2/zyp1b-1* mutant seeds, Chris Franklin for supplying the SMC3 and HEI10 antibodies, Eva Wegel for microscopy support and members of the X. Feng lab for fruitful discussions on this topic. This work was supported by a BBSRC Discovery Fellowship (BB/V005774/1) awarded to C.M. and by BBSRC Institute Strategic Programme GEN (BB/P013511/1) to M.H.

Materials and methods

Plant Materials

Arabidopsis thaliana lines used in this study were wild-type Col-0 and the *zyp1a-2/zyp1b-1* null-mutant (previously characterised in (France et al., 2021)). The *zyp1a-2/zyp1b-1* line contains a CRISPR/Cas9 derived 14 base-pair deletion in exon 3 of *ZYP1A* and a T-DNA insertion in exon 3 of *ZYP1B.* Plants were grown in controlled environment rooms with 16 h of light (125 mMol cool white) at 20 °C and 8 h of darkness at 16 °C.

Immunocytology

Immunocytology of spread *Arabidopsis thaliana* pachytene cells was performed as described previously (Morgan et al., 2021; Morgan and Wegel, 2020). In brief, staged anthers were dissected from *Arabidopsis* floral buds and macerated in a 10 µl drop of digestion medium (0.4% cytohelicase,

348 1.5% sucrose, 1% polyvinylpyrolidone in sterile water) on a No. 1.5H coverslip (Marienfeld).
349 Coverslips were then incubated in a moist chamber at 37 °C for 4 minutes before adding 10 µl of 2%
350 lipsol solution followed by 20 µl of 4% paraformaldehyde (pH 8). Coverslips were dried for 3 hours in
351 the fumehood and then blocked in blocking buffer (0.3% BSA in 1 x PBS) for 15 minutes. 50 µl of
352 primary antibody, diluted in blocking buffer, was added to the coverslips and they were then
353 incubated overnight in a moist chamber at 4 °C. 50 µl of secondary antibody, diluted in blocking
354 buffer, was added to the coverslips and they were then incubated in a moist chamber at 37 °C for 2
355 hours. Coverslips were then incubated in 10 µl DAPI (10 µg/ml) for 5 min before adding 7 µl of
356 Vectashield and mounting them on a glass slide. Coverslips were washed for 3 x 5 minutes in 1 X PBS
357 0.1% Triton before and after each incubation step. The following primary antibodies were used at
358 1:500 dilutions: anti-SMC3 (rat) (Ferdous et al., 2012) and anti-HEI10 (rabbit) (Lambing et al., 2015).
359 The following secondary antibodies were used at 1:200 dilutions: anti-rat Alexa Fluor Plus 488
360 (ThermoFisher A48262), anti-rabbit Alexa Fluor 555 (ThermoFisher A21428). Immunostained cells
361 were imaged using 3D structured illumination microscopy (3D-SIM) on a Zeiss Elyra PS1 microscope
362 equipped with an EM-CCD camera, a Plan-Apochromat ×63, NA 1.40 oil objective and 405, 488, 561
363 and 642 nm solid-state laser diodes. Cells were imaged with three stripe angles and five phases and
364 z-stacks were captured at an interval size of 0.0909 µm. An immersion oil with a refractive index of
365 1.515 was used that was optimised for the green/red (SMC3/HEI10) channels of our system. For
366 optimal image quality and to minimise the introduction of reconstruction artefacts, microscope laser
367 power and camera gain values were manually adjusted for each cell. Bleaching and contrast of raw
368 images was assessed using the SIMcheck plugin to FIJI (Ball et al., 2015).

369 Image analysis

370 Individual axes were traced and segmented in 3-dimensions from 3D-SIM z-stacks using the SNT
371 plugin to FIJI (Arshadi et al., 2021). Traces were made using the linear SMC3 signal, which localises
372 along the meiotic axis, and 3D-skeletons of each axis-traced path were generated using SNT.
373 For *zyp1a-2/zyp1b-1* nuclei, each axial element was traced end-to-end to generate 10 complete
374 skeleton traces for each nucleus. For wild-type nuclei, due to the proximity of the two parallel SMC3
375 signals, a single trace was used to segment the paths of each pair of synapsed axial elements,
376 generating 5 complete skeleton traces for each nucleus. Each wild-type trace was then doubled (to
377 give 10 traces per cell, 2 per CP) to allow the wild-type data to run through an identical analysis
378 pipeline as the *zyp1a-2/zyp1b-1* data. Foci were detected within images using the FociPicker3D Fiji
379 plugin (Du et al., 2011). Uniform background intensity thresholds and minimum pixel size values
380 were manually optimised within a range of 6,000-20,000 and 5-20, respectively, with otherwise
381 default parameters. Further analysis was performed using custom Python scripts.
382 Foci were assigned to the CP for which the maximum of the two distances from the closest points on
383 each of the axes was smallest, provided this was less than a threshold distance (0.5 µm). If this was
384 not the case, then the foci was assigned to the closest CP, provided that it was nearer to one of the
385 two axes than a smaller threshold (0.3 µm). Foci satisfying neither of these two criterion were
386 considered as off target signal and ignored. Relative positions along CPs were calculated by dividing
387 the distance along the traced axis (measured in termsof voxels) by the total length of the trace. Foci
388 intensities were calculated using the mean intensity within a sphere of radius 0.1985 µm (5 voxels in
389 the x and y planes), centred at the foci peak, and the median intensity of the image (used as an
390 estimate of the background fluorescence) was subtracted. All intensity values used were normalized
391 by dividing the foci intensity by the mean of the intensitiesof all foci within the same cell (only
392 considering foci associated with a CP). Simple linear regression was performed using the Python
393 statsmodels package.

Mathematical model

In each cell, $Q = 5$ chromosome pairs (CPs) are simulated. The q-th CP is taken to have a length L_q, sampled from the (per-chromosome) normal distribution $\mathcal{N}_T(\mu_q, \sigma_q^2, -3,3)$ truncated at 3 standard deviations from the mean (to ensure positive CP lengths). We use the same values as in our earlier cis-coarsening model, fitted to experimentally measured wild-type chromosome length distributions: $\mu_1 = 37.5, \mu_2 = 40.4, \mu_3 = 45.7, \mu_4 = 53.8, \mu_5 = 59.8$, and $\sigma_1 = 4.93, \sigma_2 = 5.06, \sigma_3 = 5.86, \sigma_4 = 7.18, \sigma_5 = 7.13$, with all these parameters having units of μm. We chose to retain these original values as they were broadly consistent with the experimental chromosome lengths measured in this study, but were calculated from a much greater sample size.

Recombination intermediates (RIs) are placed randomly along each of the CPs, with a probability ρ per µm. To implement this, for each simulated CP with length L, a random number is generated from a Poisson process with mean ρL, and then this many RIs are placed uniformly at random along that CP. We note that this procedure differs slightly from the method used in our original cis-coarsening model, where floor(ρL) crossovers were placed on a chromosome with length L. Simulation outputs with this original rule (not shown) differ only slightly from those in Figures 2 and 4.

The pro-crossover factor HEI10 is present in a nucleoplasmic pool, with amount P, and at compartments at each of the RIs, with amounts $C_{q,n}$, $1 \le q \le \mathrm{Q} = 5$, $1 \le n \le N_q$ for n-th RI on the q-th CP. HEI10 is able to move between the nucleoplasmic pool to each of the RI compartments at rate α, and to escape from the RI compartments back into the pool at a rate $\beta(C_{q,n})$, which depends on the amount of HEI10 within each individual RI compartment. As in our cis-interference model, we take

$$\beta(C_{q,n}) = \frac{\beta_C}{1 + (C_{q,n}/K)^{\gamma}}.$$

The system of ordinary differential equations governing HEI10 amounts is

$$\frac{\mathrm{d}C_{q,n}}{\mathrm{d}t} = \alpha P - \beta(C_{q,n})C_{q,n}, \qquad 1 \le q \le Q,\ 1 \le n \le N_q,$$

$$\frac{\mathrm{d}P}{\mathrm{d}t} = -\left(\sum_{q=1}^{Q} N_q\right)\alpha P + \sum_{q=1}^{Q}\sum_{n=1}^{N_q} \beta(C_{q,n})C_{q,n}.$$

This system conserves the total amount of HEI10 within each cell (the nucleoplasmic pool plus all RI compartments), rather than within each SC, which was the case for the cis-interference model.

The initial amounts of HEI10 at each of the RIs are taken to be

$$C_{q,n} = f\left(\frac{x_{q,n}}{L_q}\right)X_{q,n}, \qquad X_{q,n} \sim \mathcal{N}_T(C_0, \sigma^2, -3,3), \qquad 1 \le q \le Q,\ 1 \le n \le N_q,$$

where $\mathcal{N}_T$ again denotes a truncated normal distribution and $X_{q,n}$ is the position of the n-th RI on the q-th CP. The piecewise function $f(x/L)$, included to account for the increased frequency of crossovers towards the end of each chromosome, is defined as

$$F(\xi) = \begin{cases} 1 + (f_e - 1)(1 - \xi/x_e) & 0 \le \xi \le x_e, \\ 1 & x_e \le \xi \le 1 - x_e, \\ 1 + (f_e - 1)(\xi - 1 + x_e)/x_e & 1 - x_e \le \xi \le 1. \end{cases}$$

428 The initial amount of HEI10 within the nucleoplasmic pool is the same for all cells, $P = P_0$. To relate
429 these simulations to the cis-interference model, P_0 is taken to be (approximately) the average
430 amount of HEI10 loaded onto all the SCs in that model.

431 This system is simulated for a duration $T = 10$hr. Numerical simulations are performed using the
432 Rodas5 solver (di Marzo, 1992) of the DifferentialEquations.jl Julia package (Rackauckas and Nie,
433 2017), with a non-negativity constraint on HEI10 amounts. The initial conditions for the simulation
434 are random, but the evolution of the system is deterministic. Multiple simulations (10000) with
435 different random initial conditions are performed to determine the distribution of crossover
436 numbers, positions and intensities. At the end of each simulation, RIs are designated as crossover
437 sites if the amount of HEI10 at that RI is more than a threshold $H = 10$.

438 All parameters were chosen to be the same as those as in the cis-coarsening model, except for the RI
439 HEI10 absorption rate α, and the (maximum) escape rate β_C, which were both multiplied by a factor
440 of approximately 0.08 in order to reflect that HEI10 is now being exchanged with the nucleoplasmic
441 pool, rather than locally on the synaptonemal complex.

442 Data Availability

443 Imaging data associated with this study will be uploaded to the BioImage Archive. Custom Python
444 scripts for data analysis will be made available on GitHub.

445

446 References

447 Agarwal S, Roeder GS. 2000. Zip3 Provides a Link between Recombination Enzymes and
448 Synaptonemal Complex Proteins. *Cell* **102**:245–255. doi:https://doi.org/10.1016/S0092-
449 8674(00)00029-5

450 Arshadi C, Günther U, Eddison M, Harrington KIS, Ferreira TA. 2021. SNT: a unifying toolbox for
451 quantification of neuronal anatomy. *Nature Methods* **18**:374–377. doi:10.1038/s41592-021-
452 01105-7

453 Ball G, Demmerle J, Kaufmann R, Davis I, Dobbie IM, Schermelleh L. 2015. SIMcheck: a Toolbox for
454 Successful Super-resolution Structured Illumination Microscopy. *Scientific Reports* **5**:15915.
455 doi:10.1038/srep15915

456 Capilla-Pérez L, Durand S, Hurel A, Lian Q, Chambon A, Taochy C, Solier V, Grelon M, Mercier R.
457 2021. The synaptonemal complex imposes crossover interference and heterochiasmy in
458 Arabidopsis. *Proceedings of the National Academy of Sciences* **118**:e2023613118.
459 doi:10.1073/pnas.2023613118

460 Chelysheva L, Vezon D, Chambon A, Gendrot G, Pereira L, Lemhemdi A, Vrielynck N, le Guin S,
461 Novatchkova M, Grelon M. 2012. The Arabidopsis HEI10 is a new ZMM protein related to Zip3.
462 *PLoS Genetics*. doi:10.1371/journal.pgen.1002799

463 Colaiácovo MP, MacQueen AJ, Martinez-Perez E, McDonald K, Adamo A, la Volpe A, Villeneuve AM.
464 2003. Synaptonemal Complex Assembly in C. elegans Is Dispensable for Loading Strand-
465 Exchange Proteins but Critical for Proper Completion of Recombination. *Developmental Cell*
466 **5**:463–474. doi:10.1016/S1534-5807(03)00232-6

467 di Marzo GA. 1992. Méthodes de Rosenbrock d'ordre 5(4) adaptées aux problemes différentiels-
468 algébriques.

469 Drouaud J, Mercier R, Chelysheva L, Bérard A, Falque M, Martin O, Zanni V, Brunel D, Mézard C.
470 2007. Sex-specific crossover distributions and variations in interference level along Arabidopsis
471 thaliana chromosome 4. *PLoS Genet* **3**:e106–e106. doi:10.1371/journal.pgen.0030106

472 Du G, Drexler GA, Friedland W, Greubel C, Hable V, Krücken R, Kugler A, Tonelli L, Friedl AA, Dollinger
473 G. 2011. Spatial dynamics of DNA damage response protein foci along the ion trajectory
474 of high-LET particles. *Radiat Res* **176**:706–715. doi:10.1667/rr2592.1

475 Duroc Y, Lemhemdi A, Larchevêque C, Hurel A, Cuacos M, Cromer L, Horlow C, Armstrong SJ,
476 Chelysheva L, Mercier R. 2014. The Kinesin AtPSS1 Promotes Synapsis and is Required for
477 Proper Crossover Distribution in Meiosis. *PLOS Genetics* **10**:e1004674-.

478 Ferdous M, Higgins JD, Osman K, Lambing C, Roitinger E, Mechtler K, Armstrong SJ, Perry R, Pradillo
479 M, Cuñado N, Franklin FCH. 2012. Inter-Homolog Crossing-Over and Synapsis in Arabidopsis
480 Meiosis Are Dependent on the Chromosome Axis Protein AtASY3. *PLOS Genetics* **8**:e1002507-.

481 France MG, Enderle J, Röhrig S, Puchta H, Franklin FCH, Higgins JD. 2021. ZYP1 is required for
482 obligate cross-over formation and cross-over interference in Arabidopsis. *Proceedings of the*
483 *National Academy of Sciences* **118**. doi:10.1073/pnas.2021671118

484 Giraut L, Falque M, Drouaud J, Pereira L, Martin OC, Mézard C. 2011. Genome-Wide Crossover
485 Distribution in Arabidopsis thaliana Meiosis Reveals Sex-Specific Patterns along Chromosomes.
486 *PLOS Genetics* **7**:e1002354-.

487 Gray S, Cohen PE. 2016. Control of Meiotic Crossovers: From Double-Strand Break Formation to
488 Designation. *Annual Review of Genetics*. doi:10.1146/annurev-genet-120215-035111

489 Haldane JBS. 1931. The Cytological Basis of Genetical Interference. *CYTOLOGIA* **3**:54–65.
490 doi:10.1508/cytologia.3.54

491 Hunter N. 2015. Meiotic Recombination: The Essence of Heredity. *Cold Spring Harb Perspect Biol*
492 **7**:a016618. doi:10.1101/cshperspect.a016618

493 Jahns MT, Vezon D, Chambon A, Pereira L, Falque M, Martin OC, Chelysheva L, Grelon M. 2014.
494 Crossover Localisation Is Regulated by the Neddylation Posttranslational Regulatory Pathway.
495 *PLOS Biology* **12**:e1001930-.

496 Jantsch V, Pasierbek P, Mueller MM, Schweizer D, Jantsch M, Loidl J. 2004. Targeted gene knockout
497 reveals a role in meiotic recombination for ZHP-3, a Zip3-related protein in Caenorhabditis
498 elegans. *Mol Cell Biol* **24**:7998–8006. doi:10.1128/MCB.24.18.7998-8006.2004

499 Jones GH, Franklin FCH. 2006. Meiotic Crossing-over: Obligation and Interference. *Cell* **126**:246–248.
500 doi:https://doi.org/10.1016/j.cell.2006.07.010

501 Lake CM, Nielsen RJ, Guo F, Unruh JR, Slaughter BD, Hawley RS. 2015. Vilya, a component of the
502 recombination nodule, is required for meiotic double-strand break formation in Drosophila.
503 *Elife* **4**:e08287. doi:10.7554/eLife.08287

504 Lam WS, Yang X, Makaroff CA. 2005. Characterization of Arabidopsis thaliana SMC1 and SMC3:
505 evidence that AtSMC3 may function beyond chromosome cohesion. *Journal of Cell Science*
506 **118**:3037–3048. doi:10.1242/jcs.02443

507 Lambing C, Kuo PC, Tock AJ, Topp SD, Henderson IR. 2020. ASY1 acts as a dosage-dependent
508 antagonist of telomere-led recombination and mediates crossover interference in Arabidopsis.
509 *Proceedings of the National Academy of Sciences* **117**:13647–13658.
510 doi:10.1073/pnas.1921055117

511 Lambing C, Osman K, Nuntasoontorn K, West A, Higgins JD, Copenhaver GP, Yang J, Armstrong SJ,
512 Mechtler K, Roitinger E, Franklin FCH. 2015. Arabidopsis PCH2 Mediates Meiotic Chromosome
513 Remodeling and Maturation of Crossovers. *PLOS Genetics* **11**:e1005372-.

514 Mercier R, Jolivet S, Vezon D, Huppe E, Chelysheva L, Giovanni M, Nogué F, Doutriaux M-P, Horlow C,
515 Grelon M, Mézard C. 2005. Two Meiotic Crossover Classes Cohabit in Arabidopsis: One Is
516 Dependent on MER3,whereas the Other One Is Not. *Current Biology* **15**:692–701.
517 doi:https://doi.org/10.1016/j.cub.2005.02.056

518 Miller DE. 2020. The Interchromosomal Effect: Different Meanings for Different Organisms. *Genetics*
519 **216**:621–631. doi:10.1534/genetics.120.303656

520 Morgan C, Fozard JA, Hartley M, Henderson IR, Bomblies K, Howard M. 2021. Diffusion-mediated
521 HEI10 coarsening can explain meiotic crossover positioning in Arabidopsis. *Nature*
522 *Communications* **12**:4674. doi:10.1038/s41467-021-24827-w

523 Morgan C, Wegel E. 2020. Cytological Characterization of Arabidopsis arenosa Polyploids by SIM. In:
524 Pradillo M. HS, editor. Plant Meiosis. Methods in Molecular Biology, Vol 2061. Humana, New
525 York, NY. doi:https://doi.org/10.1007/978-1-4939-9818-0_4

526 Otto SP, Payseur BA. 2019. Crossover Interference: Shedding Light on the Evolution of
527 Recombination. *Annual Review of Genetics*. doi:10.1146/annurev-genet-040119-093957

528 Page SL, Hawley RS. 2004. THE GENETICS AND MOLECULAR BIOLOGY OF THE SYNAPTONEMAL
529 COMPLEX. *Annual Review of Cell and Developmental Biology* **20**:525–558.
530 doi:10.1146/annurev.cellbio.19.111301.155141

531 Pochon G, Henry IM, Yang C, Lory N, Jiménez NF-, Böwer F, Hu B, Carstens L, Tsai HT, Pradillo M,
532 Comai L, Schnittger A. 2022. The Arabidopsis Hop1 homolog ASY1 mediates cross-over
533 assurance and interference. *bioRxiv* 2022.03.17.484635. doi:10.1101/2022.03.17.484635

534 Prusicki MA, Keizer EM, van Rosmalen RP, Komaki S, Seifert F, Müller K, Wijnker E, Fleck C, Schnittger
535 A. 2019. Live cell imaging of meiosis in Arabidopsis thaliana. *Elife* **8**:e42834.
536 doi:10.7554/eLife.42834

537 Qiao H, Prasada Rao HBD, Yang Y, Fong JH, Cloutier JM, Deacon DC, Nagel KE, Swartz RK, Strong E,
538 Holloway JK, Cohen PE, Schimenti J, Ward J, Hunter N. 2014. Antagonistic roles of ubiquitin
539 ligase HEI10 and SUMO ligase RNF212 regulate meiotic recombination. *Nat Genet* **46**:194–199.
540 doi:10.1038/ng.2858

541 Rackauckas C, Nie Q. 2017. DifferentialEquations.jl - A performant and Feature-Rich Ecosystem for
542 Solving Differential Equations in Julia. *Journal of Open Research Software* **5**:15.
543 doi:http://doi.org/10.5334/jors.151

544 Reynolds A, Qiao H, Yang Y, Chen JK, Jackson N, Biswas K, Holloway JK, Baudat F, de Massy B, Wang J,
545 Höög C, Cohen PE, Hunter N. 2013. RNF212 is a dosage-sensitive regulator of crossing-over
546 during mammalian meiosis. *Nat Genet* **45**:269–278. doi:10.1038/ng.2541

547 Rog O, Köhler S, Dernburg AF. 2017. The synaptonemal complex has liquid crystalline properties and
548 spatially regulates meiotic recombination factors. *Elife* **6**:e21455. doi:10.7554/eLife.21455

549 Stauffer WT, Zhang L, Dernburg A. 2019. Diffusion through a liquid crystalline compartment
550 regulates meiotic recombinationProc.SPIE. doi:10.1117/12.2513378

551 Sturtevant AH. 1915. The behavior of the chromosomes as studied through linkage. *Zeitschrift für*
552 *Induktive Abstammungs- und Vererbungslehre*. doi:10.1007/BF01792906

553 Termolino P, Falque M, Aiese Cigliano R, Cremona G, Paparo R, Ederveen A, Martin OC, Consiglio FM,
554 Conicella C. 2019. Recombination suppression in heterozygotes for a pericentric inversion
555 induces the interchromosomal effect on crossovers in Arabidopsis. *The Plant Journal* **100**:1163–
556 1175. doi:https://doi.org/10.1111/tpj.14505

557 Varas J, Graumann K, Osman K, Pradillo M, Evans DE, Santos JL, Armstrong SJ. 2015. Absence of
558 SUN1 and SUN2 proteins in Arabidopsis thaliana leads to a delay in meiotic progression and
559 defects in synapsis and recombination. *The Plant Journal* **81**:329–346.
560 doi:https://doi.org/10.1111/tpj.12730

561 von Diezmann L, Rog O. 2021. Let's get physical – mechanisms of crossover interference. *Journal of*
562 *Cell Science* **134**. doi:10.1242/jcs.255745

563 Wayne C, Chloe G, Andrew L. 2021. Crossover interference: Just ZYP it. *Proceedings of the National*
564 *Academy of Sciences* **118**:e2103433118. doi:10.1073/pnas.2103433118

565 Zhang L, Köhler S, Rillo-Bohn R, Dernburg AF. 2018. A compartmentalized signaling network
566 mediates crossover control in meiosis. *Elife* **7**:e30789. doi:10.7554/eLife.30789

567 Zhang L, Stauffer W, Zwicker D, Dernburg AF. 2021. Crossover patterning through kinase-regulated
568 condensation and coarsening of recombination nodules. *bioRxiv* 2021.08.26.457865.
569 doi:10.1101/2021.08.26.457865

570 Zickler D, Kleckner N. 2016. A few of our favorite things: Pairing, the bouquet, crossover interference
571 and evolution of meiosis. *Seminars in Cell and Developmental Biology*.
572 doi:10.1016/j.semcdb.2016.02.024

573 Ziolkowski PA, Underwood CJ, Lambing C, Martinez-Garcia M, Lawrence EJ, Ziolkowska L, Griffin C,
574 Choi K, Franklin FCH, Martienssen RA, Henderson IR. 2017. Natural variation and dosage of the
575 HEI10 meiotic E3 ligase control Arabidopsis crossover recombination. *Genes and Development*.
576 doi:10.1101/gad.295501.116

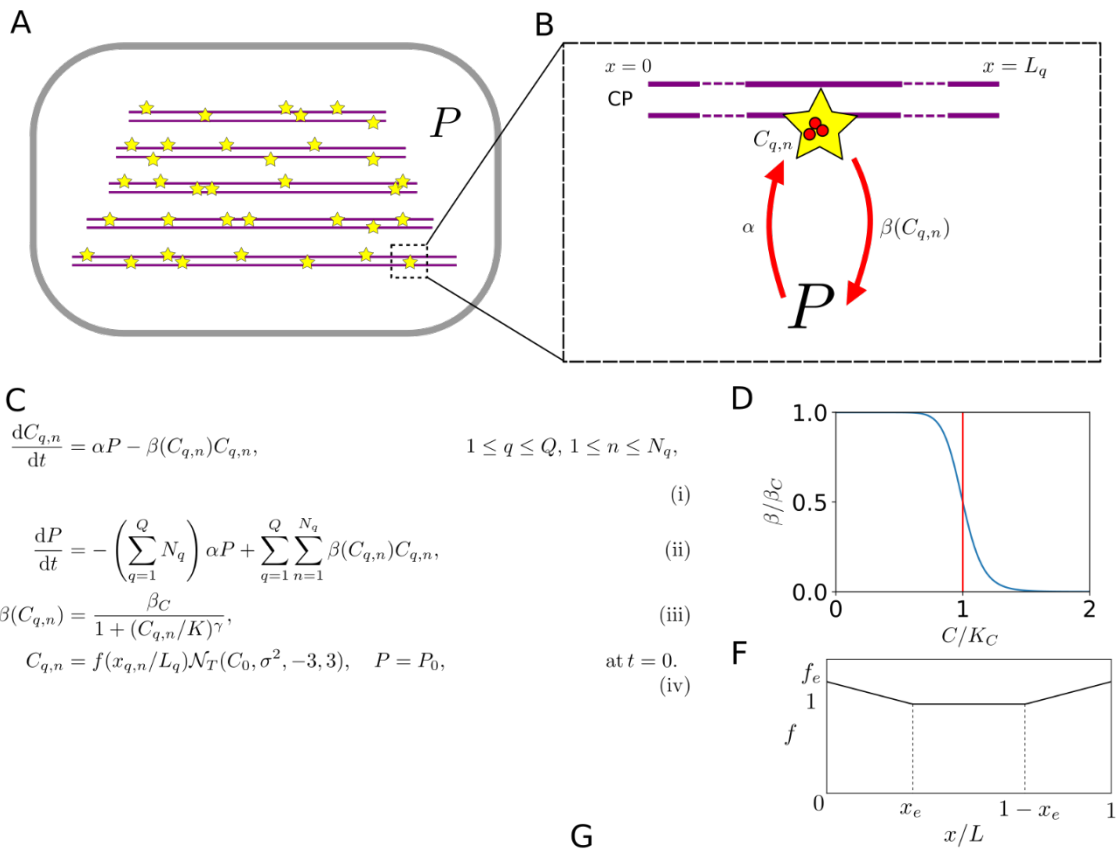

E

α	0.17 s^{-1}	RI HEI10 absorption rate
β_C	0.04 s^{-1}	RI HEI10 escape rate
γ	1.25	Escape rate Hill coefficient
K	1 au	Hill function threshold
C_0	6.8 au	HEI10 initial RI loading
σ	2.2 au	Noise in HEI10 RI loading
x_e	0.3	Telomere length (fraction of CP)
f_e	1.25	Telomere weighting for RI loading
P_0	290	Initial HEI10 in nucleoplasmic pool
ρ	0.5 μm^{-1}	Average RI density along CPs
T	36000 s	Simulation duration

G

L_q	Length of the q-th chromosome pair (CP)
P	Amount of HEI10 in nucleoplasmic pool
$C_{q,n}$	Amount of HEI10 in the n-th RI on the q-th CP
$x_{q,n}$	Distance of n-th RI along the q-th CP
q	Chromosome pair index $1 \le q \le Q = 5$
n	RI index along CP
N_q	Number of RIs on q-th CP

Figure 1. Mathematical model for HEI10 dynamics in a *zyp1* SC mutant. (**A**) Each cell contains Q=5 chromosome pairs (purple line pairs). RIs (yellow stars) are placed randomly along the chromosome pairs (CPs) immersed in the nucleoplasm (P). (**B**) HEI10 (red) is able to move from the nucleoplasmic pool into the RI compartments (rate α), and escape (rate β) from the RI compartments back into the pool. $C_{q,n}$ is the HEI10 molecule number at the n-th RI on the q-th CP, which has length L_q. (**C**) (i)+(ii) Differential equations governing nucleoplasmic pool (P) and RI HEI10 (C) amounts. (iii) Functional form of escape rate function $\beta(C)$. (iv) Initial conditions for RI and pool HEI10 amounts. $\mathcal{N}_T$ is a Normal distribution, truncated at three standard deviations away from its mean. (**D**) Graph showing RI escape rate function $\beta(C)$. (**E**) Default simulation parameter values. (**F**) Form of end-bias function f. (**G**) Description of terms appearing in model equations.

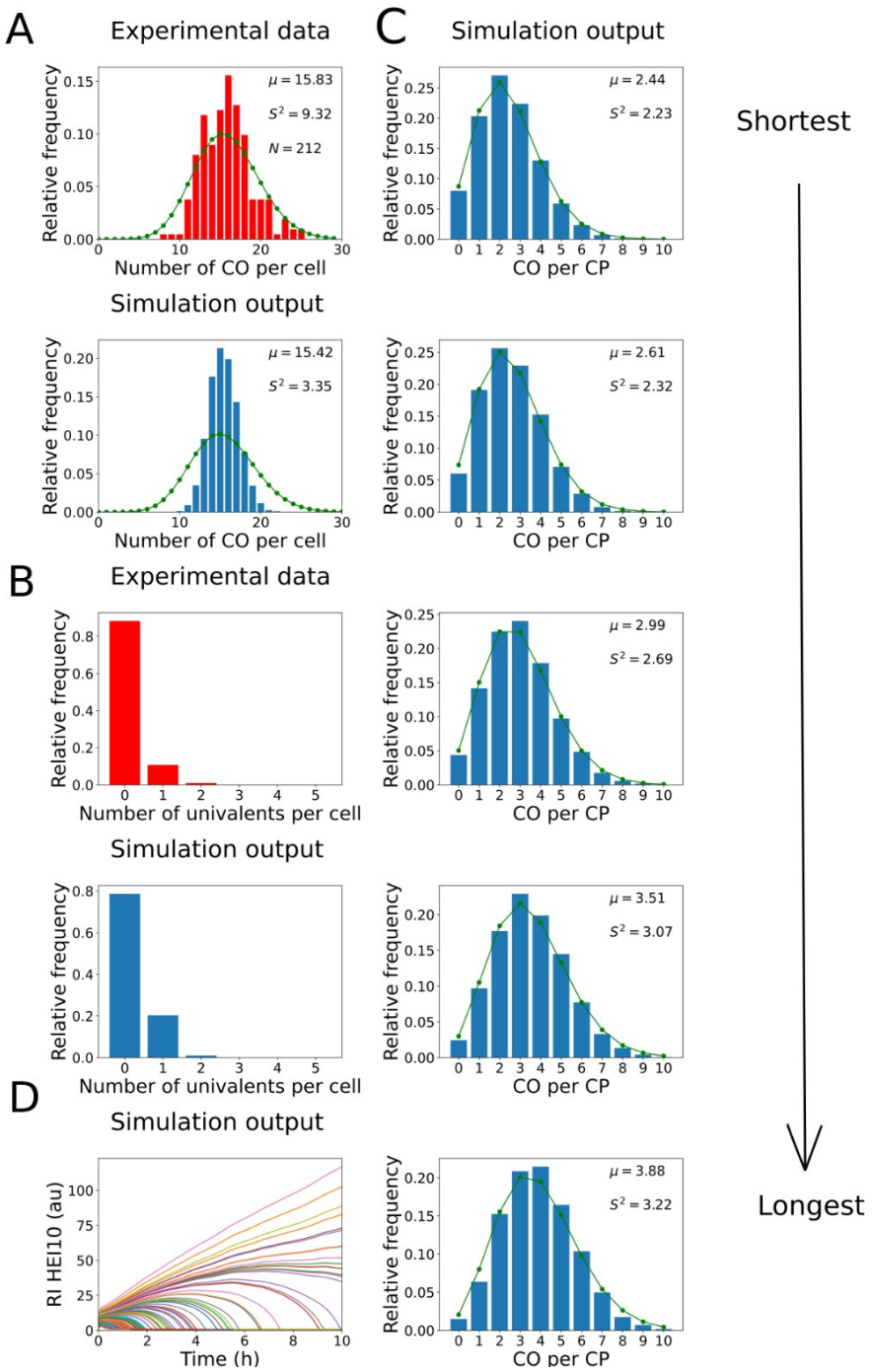

Figure 2. Analysis of CO number. (A-B) Experimental data from *zyp1* null mutant plants (top) and nucleoplasmic coarsening model simulations (bottom). Results from simulating the model for 10000 cells are shown. (**A**) Distribution of total-CO number per cell. Experimental data is from pooled MLH1 foci counts from (Capilla- Pérez *et al.,* 2021). Sample mean (μ), estimated variance (S^2), and sample size (N) inset. Green dots (joined by a line) shows a Poisson distribution with the same mean. (**B**) Distribution of univalent number per cell. Experimental data is from univalent counts in metaphase I chromosomes from (Capilla- Pérez *et al.,* 2021). (**C**) Simulation outputs showing the distribution of total-CO numbers on the five individual chromosomes pairs (CPs). Green dots and lines again show

607 Poisson distributions with same means as simulated data, with mean (μ) and estimated variance (S^2)
608 inset. (**D**) Traces of HEI10 focus intensity against time, for all RIs within a single simulated cell. All
609 simulation parameters are listed in Figure 1E.

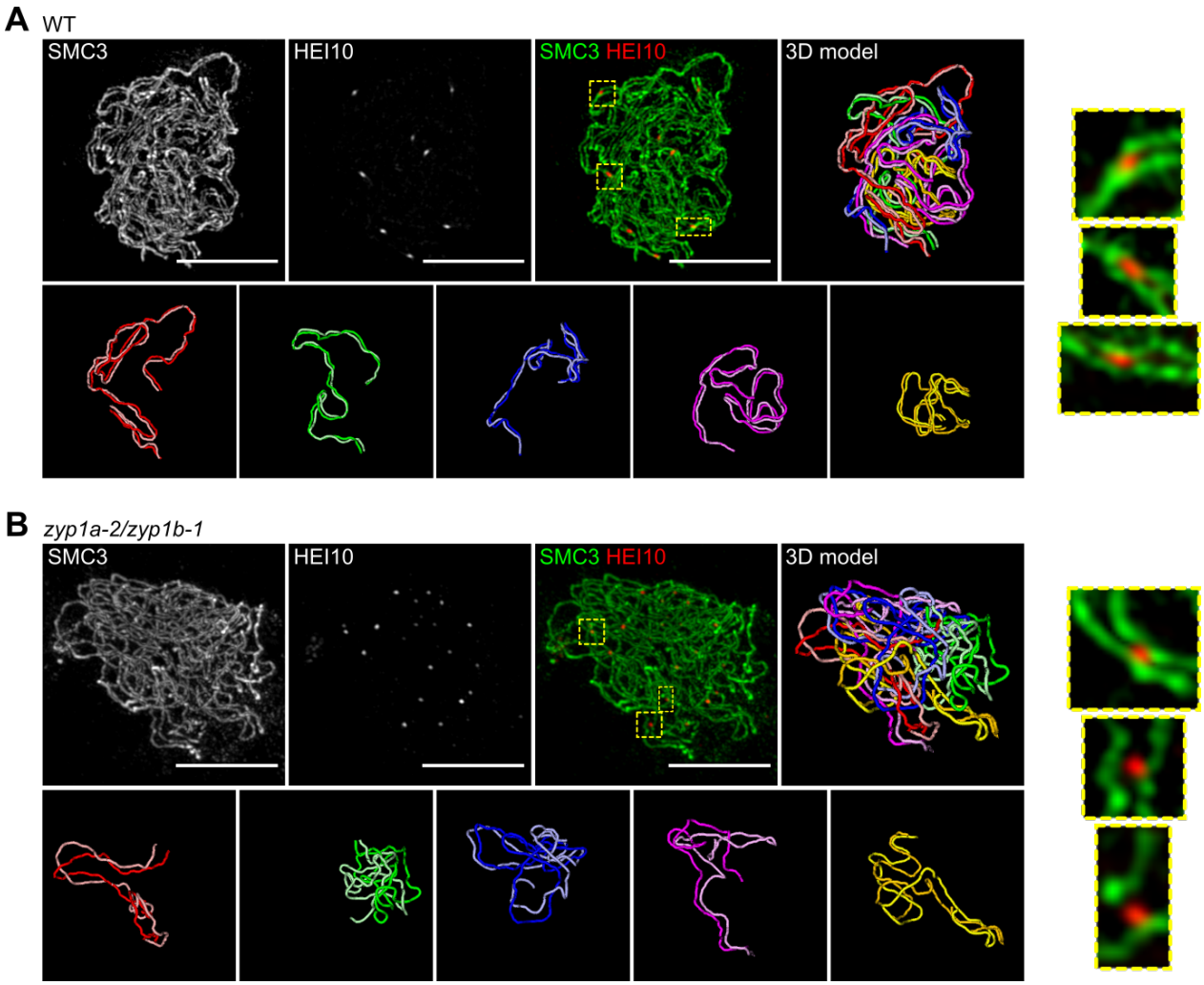

Figure 3. 3D-SIM imaging of late-prophase I cells. Maximum intensity projections of 3D-image stacks from wild-type (**A**) and *zyp1a-2/zyp1b-1* mutants (**B**), labelled for SMC3 (green) and HEI10 (red). 3D-models of segmented axial elements (with each chromosome axis labelled in a different colour), generated using the SNT plugin to FIJI, are also shown. Each nucleus contains 5 pairs of axes (*bottom row*, A, B), with individual axes in each pair having equivalent lengths and pairing tightly (A) or roughly (B) in 3D space. Zoomed in regions (*right hand panels*) from merged images (yellow dashed boxes) show the localisation of late-HEI10 foci between closely-paired axes. Scale bars = 5 µm.

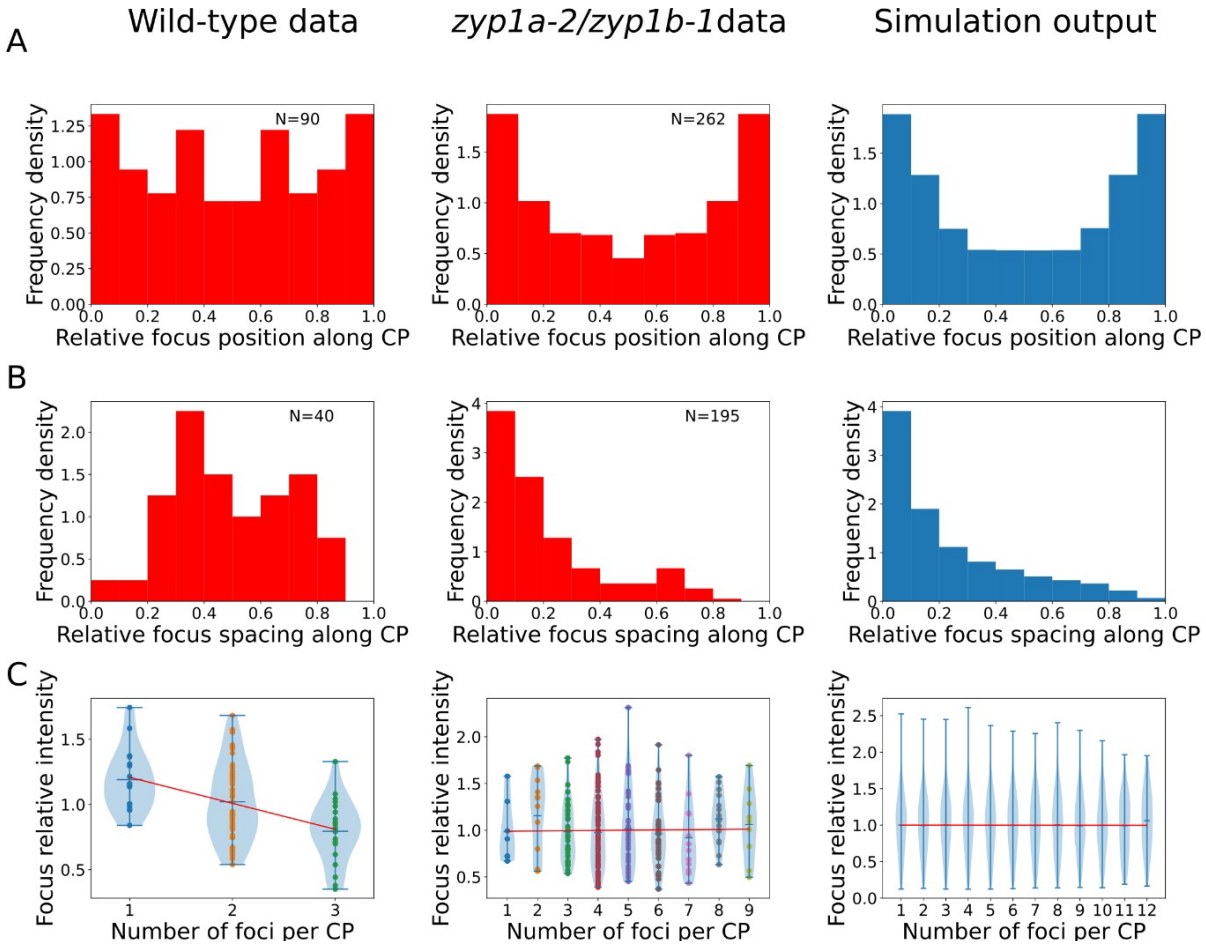

Figure 4. Analysis of late-HEI10 focus patterning and intensity data. (A-C) Experimental data from wild-type plants (left), *zyp1a-2/zyp1b-1* plants (middle), and from nucleoplasmic coarsening model simulation outputs (right). Model outputs from simulating 10000 cells are shown. (**A**) Late-HEI10 focus positions along chromosome pairs (CP), relative to the length of the CP. Experimental data are replicated and made symmetric about CP midpoints. (**B**) Distribution of spacing between adjacent late-HEI10 foci, relative to the length of the CP. (**C**) Violin plots of late-HEI10 foci intensities against the number of late-HEI10 foci on that CP. Focus intensities are relative to the mean intensity of all (on-CP) HEI10 foci within the same cell. Red lines show simple linear regression best fits, treating the number of foci on the CP as a continuous independent variable. For wild-type plants, slope = -0.1944, R^2=0.188, F(1,88)=20.36, p<0.001. For *zyp1* mutant plants, slope=0.0028, R^2<0.001, F(1,260)=0.04538, p=0.831. For simulated data, slope=-0.0003, R^2<0.001, F(1,154228)=0.3030, p=0.582. Simulation parameters are again as listed in Figure 1E.